Boron Enhanced Synthesis of Ti-hydride Nanoparticles by Milling Ti/B in Hydrogen Flow

C. Borchers[1], T.I. Khomenko[2]*, A.V. Leonov[3], O.S. Morozova[2], J. Cizek[4], I. Prochazka[4], A.S. Shkvarin[5], E.Z. Kurmaev[5] and A. Moewes[6]

[1]*Institute for Material Physics, University of Göttingen, Friedrich-Hund-Platz 1, 37077 Goettingen, Germany,* [2]*Semenov Institute of Chemical Physics RAS, 4 Kosygin St. 119991 Moscow, Russia,* [3]*Department of Chemistry, Lomonosov Moscow State University, Leninskie Gory, 119899 Moscow, Russia,* [4]*Faculty of Mathematics and Physics, Charles University in Prague, V Holesovickach 2, CZ18000 Praha 8, Czech Republic,* [5]*Institute of Metal Physics, RAS-Ural Division, 18 Kovalevskaya St, 620041 Ekaterinburg, Russia,* [6]*Department of Physics and Engineering Physics, University of Saskatchewan, 116 Science Place, Saskatoon, Saskatchewan S7N 5E2, Canada*

Abstract: Morphological, structural and chemical evolution in Ti/B/H_2 system is studied in detail as a function of mechanical treatment. Ti/B powder continuously changes both in composition and morphology during ball-milling in H_2 flow: The powder composition varies from Ti/B to TiH_{2-x}/B causing a change in mechanical properties. The role of boron additive also changes from preventing the Ti nanoparticles from sticking together in the early stages to a matrix material participating in Ti – B interface reactions in the intermediate and final stages of the process. Boron atoms participating in the formation of nanoscopic holes give rise to new H states in the hydride by changing the local atomic state of Ti atoms. The dynamics of the formation of these sites and the redistribution of hydrogen between different types of occupation sites in dependence of phase composition and milling time of the powders are also studied.

Keywords: Mechanochemical synthesis, nanoscopic holes, positron annihilation spectroscopy, titanium hydride, X-ray emission spectroscopy, transmission electron microscopy.

1. INTRODUCTION

Hydrogen storage is one of the most important issues in developing a hydrogen economy. The storage in form of hydrides bears several positive aspects: Unlike pure hydrogen, hydrides are safe to handle, and the hydrogen density is high. However, since most metal hydrides are thermodynamically quite stable, high temperatures and long times are needed to charge and release the hydrogen, an aspect that is in most prospective applications rather unfavorable. One path to overcome this problem is to reduce the hydride particle size to the nanometer range, e.g. by mechanical milling.

Mechanochemical synthesis is widely used to ease manufacturing of different inorganic compounds from elements, including metal hydrides [1-6]. Ball-milling stimulates solid state and gas–solid reactions by decreasing the size of the intermixing reactants and increasing the number of chemically active surface and bulk sites. Mechanical energy, the driving force for mechanically stimulated synthesis, is stored in form of strain and defects (grain boundaries, dislocations, vacancies) introduced into the lattice of powder particles [7]. As a result, the juvenile powder surface formed during ball milling significantly enhances gas–solid reactivity. Concurrently, gas transportation from the surface to the bulk is faster along the new grain boundaries. A highly reactive fine metal powder can be easily prepared by milling with additives, such as carbon or liquids with surfactant properties [8-10].

Titanium hydride has been an attractive material for the purpose of hydrogen storage [11]. The approach to mechanochemical synthesis of Ti-hydride presented in this work is to use solid additives as matrix forming material containing nanosized Ti and TiH_{2-x} particles. A basically inert matrix protects fresh Ti-hydride nanofragments from atmospheric impact but assures hydrogen access to the fresh surface of Ti nanofragments. Ball-milling of Ti and graphite in H_2 is a highly effective technique to synthesize nanocrystalline Ti-hydride powder [3,6,12,13]. However, the formation of a TiC surface layer can block the Ti surface and suppress the Ti–H_2 interaction [12,13]. The application of other materials, in particular boron, to promote the mechanochemical synthesis of metal hydrides is poorly studied. Dobrovol'skii and co-workers studied the Ti-B-H sytem where TiH_2 was the hydrogen source and found a marked reduction in thermal stability of the hydride [14]. Fang and co-workers observed in situ formation and rapid decomposition of titanium tetrahydroborate $Ti(BH_4)_3$ by mechanical milling $LiBH_4$ with TiF_3 [15]. Since the titanium tetrahydroborate decomposes at temperatures beneath 100 °C without undesired hydrogen impurities [15,16], boron seems to be an additive that is worth studying.

The aim of this work is to study in detail morphological, structural and chemical evolution in Ti-B-H_2 system as a function of mechanical treatment.

2. EXPERIMENTAL

Starting powders are elemental titanium with a purity of 99.5 % consisting of spherical particles of about 200 μm in diameter with a specific surface area S = 0.015 m^2/g as well as amorphous boron with a purity of about 99 % and S = 5.4 m^2/g.

The synthesis of Ti/B nanocomposites was carried out at room temperature and atmospheric pressure in a flow mechanochemical reactor with an average energy intensity of 1.0 W/g. The stainless-steel container was loaded with 1.8 g of reaction mixture (1.5 g Ti and 0.3 g B, S = 0.9 m^2/g) together with 19.8 g of hardened steel balls of 3 – 5 mm in diameter. Hydriding experiments were carried out in a gas flow containing 55 vol. % H_2/He at a flow rate of 8 – 10 ml/min. Hydrogen absorption and effluent gas composition were continuously monitored by a gas-chromatograph combined on-line with the milling device. The interval of mechanochemical treatment was 15 – 206 min. The samples will in the following be called Ti/B_{15} ... Ti/B_{206} with the milling time as subscript.

The specific surface area S was measured by low-temperature Ar adsorption. Microstructure and morphology of the powders were characterized by scanning electron microscopy (SEM) using a micro probe Cameca MBX-1M, and by transmission electron micros-

*Address correspondence to this author at the Institute for Material Physics, University of Göttingen, Friedrich-Hund-Platz 1, 37077 Goettingen, Germany; Tel.: +49-551-395584; Fax: +49-551-395012;
E-mail: chris@ump.gwdg.de

1573-4137/11 $58.00+.00

copy (TEM) as well as high resolution transmission electron microscopy (HREM) using a Philips CM 200 UT at an acceleration voltage of 200 kV. Samples for TEM and HREM were prepared in an ethanol suspension and placed on copper grids covered by amorphous carbon. Phase composition and structural characteristics were studied by X-ray diffraction (XRD) of as-milled powders on different steps of preparation and treatments using a Dron-3 diffractometer with Cu Kα radiation. The phase composition of solids was identified using JCPDS files provided by the International Center for Diffraction Data. The hydrogen content in TiH_{2-x} is calculated after [17], where a linear relationship between the lattice constant of δTi_{2-x} and the hydrogen deficiency x is stated. The amount of hydride in the samples is calculated by using the H/Ti ratios evaluated during milling. The block size d, and microdistortions $\langle\varepsilon^2\rangle^{1/2}$ were calculated from the difference in angular dependence of the physical broadening of Ti(002) – (004) diffraction maxima. The physical broadening was determined by an approximation procedure using the same diffraction maxima of original Ti as reference values. The errors of parameters determination were $\Delta d \approx \pm 10$ % and $\Delta\langle\varepsilon^2\rangle^{1/2} \approx \pm 15$ %, respectively [18]. The deformation stacking fault probabilities in basal and prismatic planes of Ti were calculated according to [19-22].

Temperature desorption spectroscopy (TDS), which allows to evaluate hydrogen desorption and trapping characteristics, was used to characterize the hydrogen state in Ti-hydride produced during the mechanochemical treatment. The TDS measurements were carried out at a heating rate of 10 – 11°/min from 293 to 1100 K under flow conditions at a flow rate of 100 ml/min using pure Ar. A flow quartz reactor was charged with 0.1 g of testing powder. The testing powder was mixed with about 70 wt. % quartz powder in order to minimize the temperature difference between the sample and the surroundings of the reactor caused by the heat of dehydrogenation reactions and to prevent powder caking. H_2 emission was monitored continuously with a gas chromatograph, in which a thermal-conductivity detector was applied to monitor changes in hydrogen concentration in the carrier stream. The amount of hydrogen emitted was calculated by integrating the area under the TDS curves.

Positron annihilation spectroscopy (PAS) was carried out for the samples Ti/B_{66}, Ti/B_{206}, and additionally, for pure B powder as well as TiH_2/B milled for 66 min in He. For PAS, a $^{22}Na_2CO_3$ positron source with an activity of 1.5 MBq deposited on a 2 μm thick mylar foil was used. The source was placed in the center of a small cylindrical chamber with a diameter of 8 mm and a height of 5 mm. Subsequently, the chamber was completely filled with the measured powder and closed. Dimensions of the chamber ensure that virtually all positrons are thermalized inside the chamber and, thereby, annihilate in the studied powder.

Positron lifetime (PL) measurements were performed on a digital PL spectrometer described in Refs. [23,24]. The spectrometer is equipped with BaF_2 scintillators and fast photomultipliers Hamamatsu H3378. Detector pulses are directly digitized using a couple of 8-bit ultra-fast digitizers Acqiris DC 211 with sampling frequency of 4 GHz and stored in a PC. Analysis of digitized pulses and construction of PL spectrum is performed off-line using so called integral true constant fraction technique described in Ref. [25]. The spectrometer exhibits excellent timing resolution of 145 ps (FWHM ^{22}Na). The PL spectra, which always contained at least 10^7 positron annihilation events, were decomposed using a least square fitting program LT (version 9) described in Ref. [26]. The source contribution to PL spectra consisted of two weak components with lifetimes of ~368 ps and ~1.5 ns and corresponding intensities of ~8 % and ~1 %.

X-ray emission spectra (XES) were recorded for Ti/B_{66} and Ti/B_{78} powders. For the sake of comparison, TiH_2/B and Ti/B powders milled in He flow for 66 min were also studied. We have measured Ti $L_{2,3}$ ($3d4s \rightarrow 2p$ transition), B $K\alpha$ ($2p \rightarrow 1s$ transition) X-ray emission spectra of all four samples. XES measurements were performed at Beamline 8.0.1 of the Advanced Light Source at the Lawrence Berkeley National Laboratory. The emitted radiation is collected by a Rowland circle-type spectrometer with spherical gratings and recorded with an area-sensitive multichannel detector. The total experimental resolution in the Ti x-ray emission region is 0.7 eV. All emission spectra are normalized to the number of photons falling on the sample, monitored by a highly transparent gold mesh in front of the sample.

3. RESULTS

3.1. Effect of Mechanochemical Treatment on Ti/B Powder Morphology and Microstructure

The morphology of original Ti and as-milled Ti and Ti/B powders is shown in the SEM micrographs of Fig. (**1**). The original Ti powder consists of spherical particles with a narrow size distribution. After 66 min of ball-milling of Ti in H_2/He flow without boron, deformed, flat particles, 150 – 300 μm in size, with rough surfaces were formed, see Fig. (**1**(**b**)). The small particles about 5 – 20 μm in size are most probably brittle Ti-hydride formed under the treatment. The specific surface area increased from 0.015 to 0.24 m^2/g. Fig. (**1**(**c**), and (**d**)) show Ti/B_{15}, and Ti/B_{100}. Three features, namely (i) fragmentation of titanium particles, (ii) boron powder size reduction, and (iii) covering of Ti fragments by fine boron powder partially agglomerated to an average size of about 5 μm are observed after 15 min of milling, see Fig. (**1**(**c**)). As a result, the Ti/B powder surface area is increased from 0.9 to 3.3 m^2/g. In contrast to pure Ti powder, titanium debris were prevented from agglomeration by further intermixing with the boron component. The powder milled for 100 min was 1 – 5 μm in size, see Fig. (**1**(**d**)). Its surface area S increased to 11.1 m^2/g. Fig. (**2**) shows TEM and HREM micrographs of Ti/B_{100} powders: (a) overview of a Ti/TiH_{2-x}/B nanocomposite particle. The filament-like structure is the carbon grid serving as sample-holder.

Figure. (**2**(**b**)) is a close-up, dark spots are nano-sized Ti or Ti hydride particles in a boron matrix, 2(c) is a HREM micrograph, where an ellipsoidal TiH_{2-x} particle about 4 x 8 nm in size is encircled, and the arrow points to a crystalline flake-like boron particle, 2(d) is a HREM micrograph, where the lattice fringes stem from TiH_{2-x} particles. A similar powder architecture was observed earlier for Ti/graphite and Ti/*h*-BN as-milled powders [13,27].

3.2. H_2 Uptake Under Mechanochemical Treatment And Subsequent TP Desorption

Figure. (**3**(**a**)) shows kinetics of H_2 uptake under mechanical treatment and during post-milling period for 25 and 36 min of treatment. Hydrogen sorption can be observed after about 10 min of incubation period. The total hydrogen sorption after these treatments was 1.24 x 10^{-3} mol/g Ti (H/Ti = 0.12) and 2.88 x 10^{-3} mol/g Ti (H/Ti = 0.28), respectively. The most noticeable feature of short milling treatment is a prolonged and remarkable post-milling effect: Hydrogen absorption continued for approximately 30 to 40 min after interrupting the milling and yielded 64 % and 40 % of the total uptake for 25 and 36 of milling, respectively. Table **1** summarizes the H_2 up-take data. Fig. (**3**(**b**)) shows kinetics of H_2 absorption during 51, 66 and 78 min of milling. The total hydrogen sorption after these treatments was 5.44 x 10^{-3} mol/g Ti (0.52 H/Ti), 9.1 x 10^{-3} mol/g Ti (0.87 H/Ti) and 9.98 x 10^{-3} mol/g Ti (0.96 H/Ti), respectively. The relative post-milling hydrogen sorption decreased with milling time, and was found to yield 37 %, 20 % and 13 % of the total H_2 uptake, respectively. However, the absolute post-milling uptake stayed in the same order of magnitude. Fig. (**3**(**c**)) shows kinetics of H_2 absorption during 100 min of milling. Total saturation of titanium metal by hydrogen was reached before the end of the milling, i.e. after about 90 min when 1.44 x 10^{-2} mol/g Ti (1.46 H/Ti) was absorbed.

Figure. (**4**(**a**)) shows TDS spectra recorded for Ti/B_{15}, Ti/B_{25}, and Ti/B_{36} in comparison with that recorded for original Ti powder

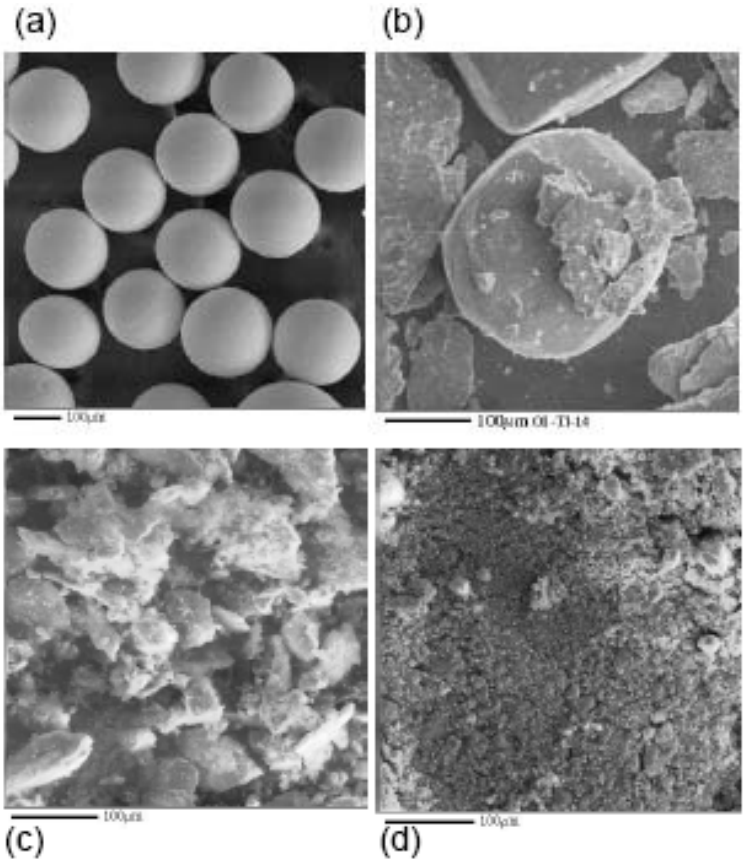

Fig. (1). SEM micrographs of original and as-milled powders: Ti - (**a**) original and (**b**) milled for 66 min in H_2/He flow; Ti/B - (**c**) milled for 15 min, and (**d**) for 100 min in H_2/He flow.

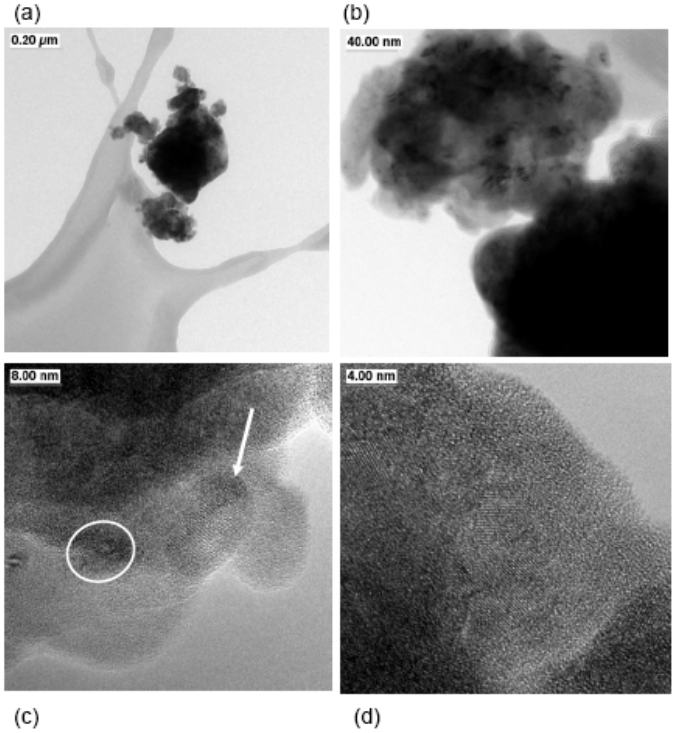

Fig. (2). TEM and HREM micrographs of Ti/B as-milled powders after 100 min of milling in H_2/He flow: (**a**) overview of $Ti/_{TiH2-x}$/B nanocomposite (**b**) close-up, dark spots are nano-sized Ti or TiH_{2-x} particles in a boron matrix, (**c**) HREM, encircled is an ellipsoidal TiH_{2-x} particle about 4 x 8 nm in size, the arrow points to a crystalline boron particle, (**d**) HREM, the lattice fringes stem fron TiH_{2-x} particles.

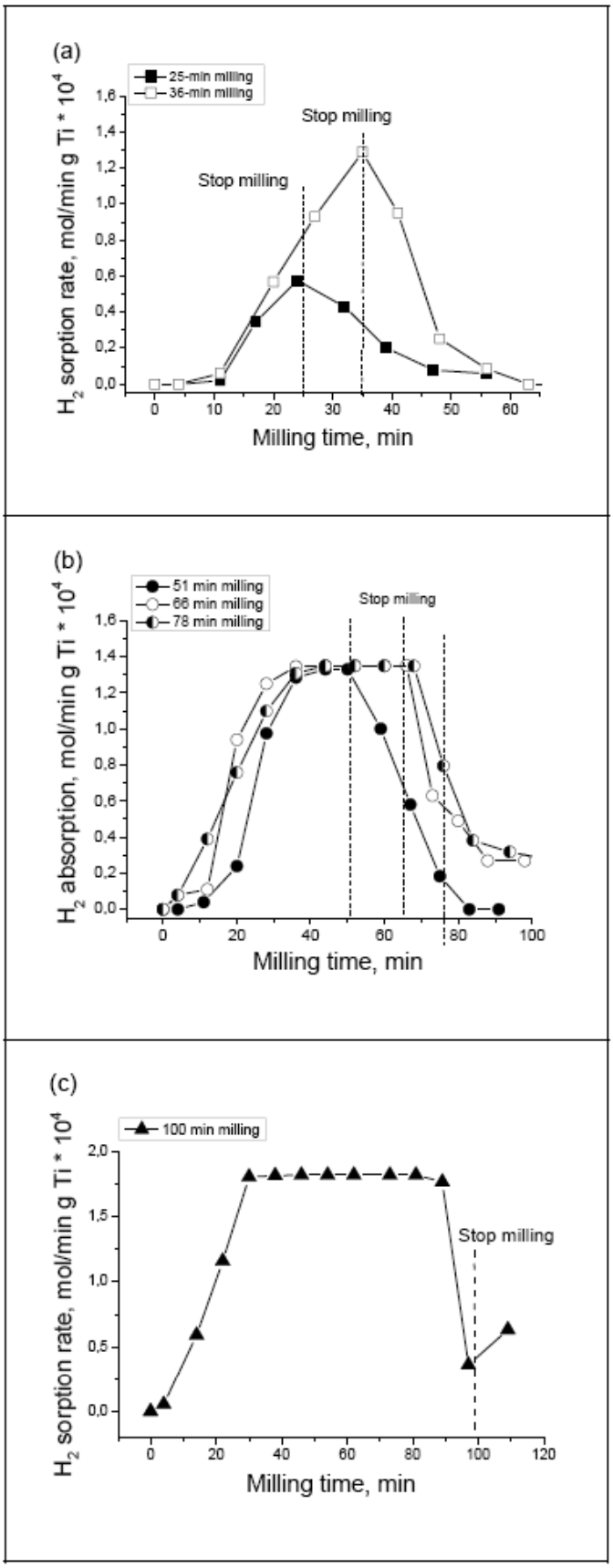

Fig. (3). Kinetics of H_2 absorption under the milling and during post-milling period: (**a**) – early stages; (**b**) – intermediate stages and (**c**) - final stage.

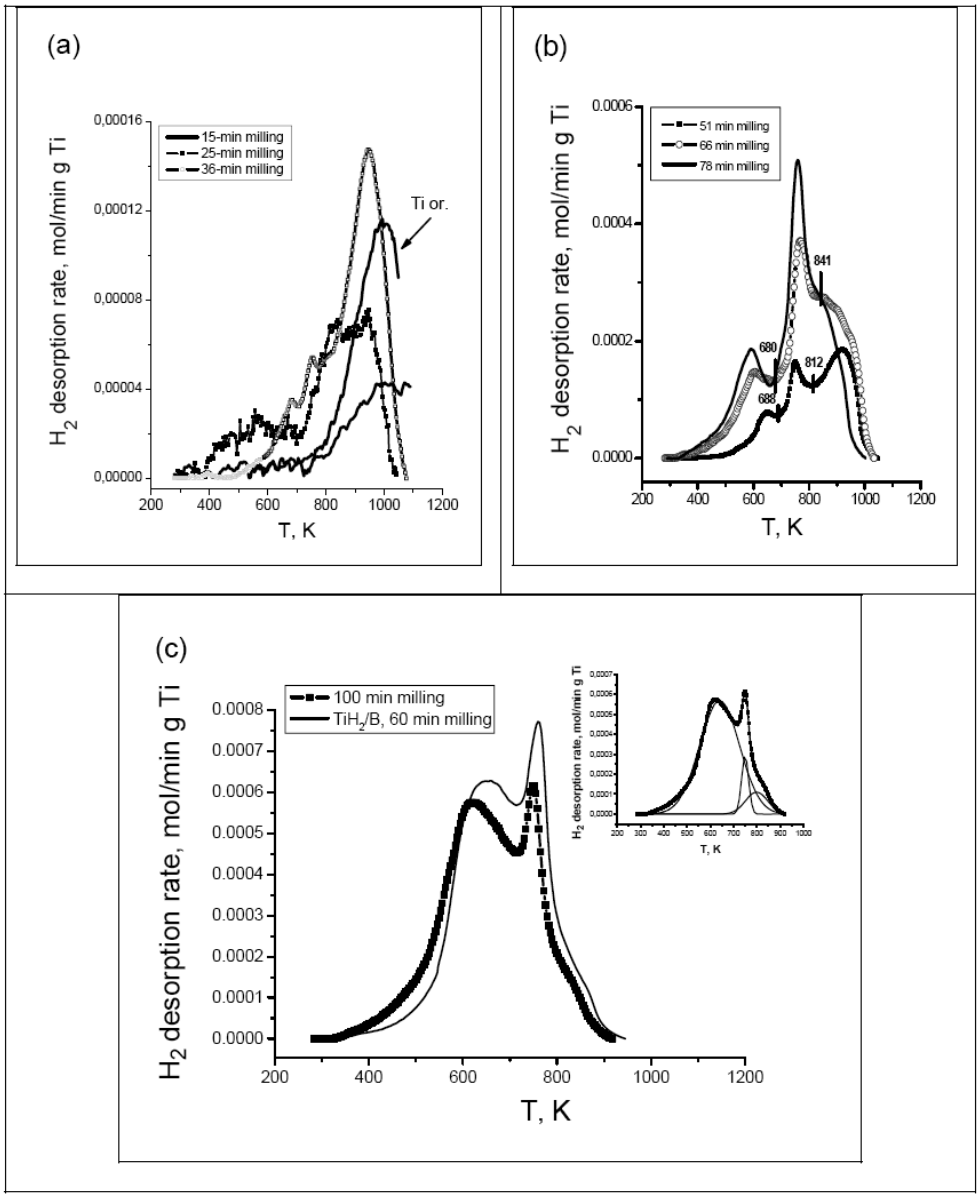

Fig. (4). TDS spectra recorded on different stages of Ti/B and H_2 interaction in comparison with that of Ti original: (**a**) – early stages; (**b**) – intermediate stages and (**c**) – final stage. Insert: an example of TDS curve Gaussian fitting.

Table 1. Effect of Milling Time on H_2 Uptake Under the Milling Conditions

Sample	Milling Time [min]	H_2 Up-take Under Milling [mol/g Ti]	H_2 Up-take in Post-effect [mol/g Ti]	Total H_2 Up-take [mol/g Ti]	H/Ti ratio
Ti/B_{15}	15	–	–	–	–
Ti/B_{25}	25	4.42×10^{-4}	7.97×10^{-4}	1.24×10^{-3}	0.12
Ti/B_{36}	36	1.73×10^{-3}	1.15×10^{-3}	2.88×10^{-3}	0.28
Ti/B_{51}	51	3.38×10^{-3}	2.06×10^{-3}	5.44×10^{-3}	0.52
Ti/B_{66}	66	7.44×10^{-3}	1.66×10^{-3}	9.1×10^{-3}	0.88
Ti/B_{78}	78	8.78×10^{-3}	1.2×10^{-3}	9.98×10^{-3}	0.96
Ti/B_{100}	100	1.42×10^{-2}		1.42×10^{-2}	1.36

milled for 66 min in H_2/He flow. The latter clearly exhibits one single peak at $T \approx 1000$ K. The sample milled for 15 min also shows one single peak at about the same maximum temperature. The TDS spectra from the powders milled for 25 and 36 min seem to be a combination of two overlapping peaks, where the high-temperature peak at 882 and 946 K has a desorption activation energy of 270.6 ± 6.6 kJ/mol in the case of Ti/B_{36}; the low-temperature peak with peak maxima 563 and 755 K has a desorption activation energy roughly estimated as 60 kJ/mol, again in the case of Ti/B_{36}. TDS parameters are summarized in Table **2**. Fig. (**4(b)**) shows TDS spectra recorded for as-milled samples Ti/B_{51}, Ti/B_{66}, and Ti/B_{78}, respectively. According to Gaussian multi-peak fitting, the curves consist of three to four overlapping peaks: One high-temperature peak at about 950 K, detected for Ti/B_{51} and Ti/B_{66}, which is not observed for Ti/B_{78}, together with a second high-temperature peak at about 850 K, which is the highest one in case of Ti/B_{78}. Then there is a peak with a maximum at about 750 K, the intensity of which increases from 10 to 30 % of the total integral intensity, as milling time increases from 51 to 78 min. A low-temperature desorption peak appears at a temperature around 600 – 650 K. The amount of hydrogen desorbed at these temperatures increases from 23 to 34 % of the total hydrogen content, as the milling time increases. The effective activation energies were estimated for this desorption step on base of TDS curve Gaussian fitting as about 60, 36, and 41 kJ/mol for milling times 51, 66, and 78 minutes, see Table **2**.

The Ti/B_{100} spectrum exhibits a remarkable resemblance to that recorded for TiH_2/B milled for 60 minutes. It should be noted that in case of Ti/B_{25}, Ti/B_{36}, Ti/B_{51}, Ti/B_{78}, and Ti/B_{100} the amount of hydrogen desorbed is smaller than the hydrogen uptake during milling. The amount of non-desorbed hydrogen is about 70 % of the total hydrogen in case of Ti/B_{25}, and 6 %, 10 %, 0.8 %, and 1.4 % in case of Ti/B_{36}, Ti/B_{51}, Ti/B_{78}, and Ti/B_{100}, respectively. However, the absolute value is below 1 x 10^{-3} mol/g Ti in all cases.

For the samples Ti/B_{51} and Ti/B_{66} the desorption process was interrupted at the temperatures indicated in Fig. (**4(b)**) in order to check the phase compositions after each of the different desorption peaks by XRD. TDS spectra recorded for Ti/B_{100} and as-milled TiH_2/B powders are shown in Fig. (**4(c)**): There is a low-temperature desorption step at 640 K, and a high-temperature double-peak at 750/799 K. As follows from Gaussian fitting of TDS curves (Fig. **4(c)**, insert), about 80 % of total H_2 content was desorbed at T_{max} = 640 K. The activation energy of this peak is E_a = 46.7 ± 0.9 kJ/mol. About 10 % of the total hydrogen content was desorbed in each of the high-temperature peaks.

3.3. XRD Results

3.3.1. After Milling

Figure. (**5(a)**) shows XRD patterns recorded from the original Ti powder, pure Ti milled for 66 minutes in H_2/He, and Ti/B_{15}, Ti/B_{25}, and Ti/B_{36}. The original Ti powder consists of hcp αTi with lattice parameters a = 0.295 nm and c = 0.469 nm. The milled powders contain αTi and titanium hydride. All Ti peaks are broadened, but there is no peak shift compared to the original peak positions. A peak shape analysis reveals that peak broadening is due to a high defect concentration and high stacking fault density in the prismatic plane – up to 8 % after 15 min of milling. The detected Ti-hydrides

Table 2. Parameters of TDS Process

Sample	T_{max} [K]	E_A [kJ/mol]	H-desorbed [mol/g Ti]
Ti/B_{15}	~ 1000		
Ti/B_{25}	563		8.7 x 10^{-5}
	882		2.8 x 10^{-4}
Ti/B_{36}	775	~ 60	1.3 x 10^{-3}
	946	270.6 ± 6.6	1.4 x 10^{-3}
Ti/B_{51}	651	60.1 ± 1.2	1.2 x 10^{-3}
	752		5.2 x 10^{-4}
	846 935	166.2 ± 2.8 363.9 ± 7.9	1.95 x 10^{-3} 1.2 x 10^{-3}
Ti/B_{66}	635	36.0 ±0.7	3.1 x 10^{-3}
	770		1.1 x 10^{-3}
	854 952	164.3 ± 2.7 470.0 ± 15.2	4.1 x 10^{-3} 8.0 x 10^{-4}
Ti/B_{78}	592	41.2 ± 0.8	2.9 x 10^{-3}
	752		2.8 x 10^{-3}
	855	148 ± 2	4.2 x 10^{-3}
Ti/B_{100}	640	46.7 ± 0.9	1.2 x 10^{-2}
	750 799	 180 ± 3	1.1 x 10^{-3} 1.1 x 10^{-3}

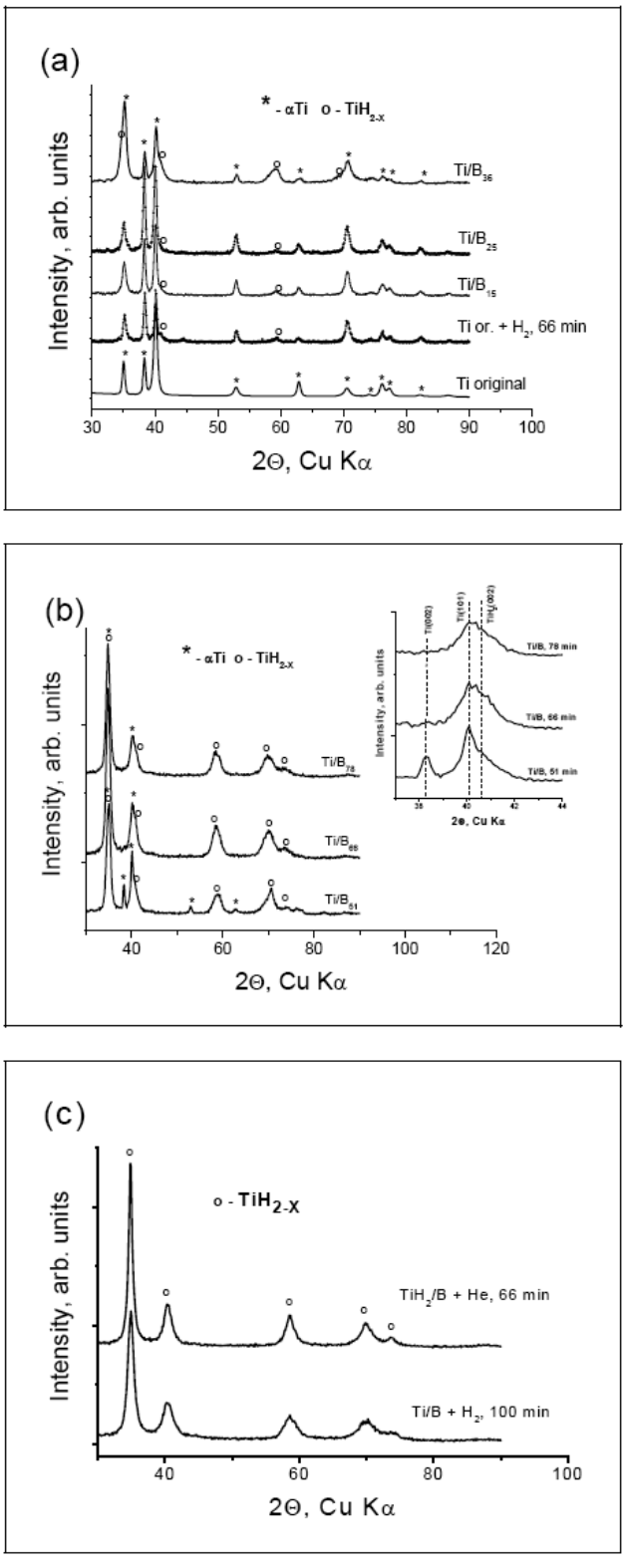

Fig. (5). XRD patterns for Ti/B powders milled in H_2/He flow: (**a**) Ti original, Ti milled for 66 min in H_2, Ti/B milled for short times, (**b**) Ti/B milled for intermediate times, (**c**) Ti/B_{100} and TiH_2/B milled for 66 min.

can be attributed to either cubic δTi_{2-x}, tetragonal εTiH_2, or a combination of both. Because of extremely broad corresponding XRD-peaks, these phases are not easy to distinguish. For the sake of simplicity, the hydrides were identified as cubic δTiH_{2-x} phase (JCPDS 25-982), the lattice constant of which ranged from a = 0.4402 – 0.4429 nm, see Table **3**, where the XRD results after milling are listed. Ti-hydride was detected in the XRD pattern after 15 minutes of milling, when the hydrogen deficiency x is about 0.45. After 25 min of milling, $TiH_{1.5}$ is present in an amount of about 18 %. In Ti/B_{36}, about 17 % of $TiH_{1.7}$ is present. Fig. (**5**(**b**)) shows XRD patterns recorded for powders milled for intermediate periods of time. Ti/B_{51} consists of two phases: αTi with an average crystallite size of about 50 nm and about 30 % of $TiH_{1.8}$ with an average crystallite size of about 5 nm. In both Ti/B_{66} and Ti/B_{78}, $TiH_{1.85}$ was formed in amounts of about 50 %. The average crystallite size was calculated by the Scherer equation for TiH_2 (200) peak as about 4 nm. XRD pattern of Ti/B powder milled for 100 min in H_2 flow is virtually the same, as that of TiH_2/B powder milled for 66 min in He flow, see Fig. (**5**(**c**)). The Ti/B_{100} sample consists of about 75 % of the cubic phase $TiH_{1.85}$ with an average crystallite size of about 4 nm.

Table 3. Effect of Milling Time on Lattice Parameters in (Ti-B)/H_2 System

Sample	Lattice Parameters [nm]		
	hcp		fcc
	a	*c*	*a*
Ti or.	0.2954	0.4693	
Ti/B_{15}	0.2958	0.4698	0.4410
Ti/B_{25}	0.2959	0.4698	0.4402
Ti/B_{36}	0.2955	0.4689	0.4429
Ti/B_{51}	0.2963	0.4692	0.4447
Ti/B_{66}			0.4459
Ti/B_{78}			0.4461
Ti/B_{100}			0.4453

3.3.2. After Thermal Desorption

Figure. (**6**) shows XRD spectra of Ti/B_{15}, Ti/B_{25}, and Ti/B_{36} after thermal desorption. Obviously, Ti hydride totally decomposed during the heating. The spectra can be interpreted as a combination of two hexagonal phases, αTi and a solid solution of H or B in Ti, identifiable by a low-angle asymmetry in XRD peaks observed after TDS, see Fig. (**6**), insert. The two phases have very close *a* and different *c* lattice constants. The solid solution accounts for roughly 20 % of the sample. A similar effect, the formation of a Ti(H) solid solution after TDS, was detected for pure Ti milled in H_2, see Fig. (**6**), insert.

To study the structural evolution during TDS, the phase composition of powders milled for 51 and 66 min was determined on different stages of interrupted TDS: 688 and 680 K as well as 812 and 841 K, respectively, as marked in Fig. (**4**(**b**)). The results are shown in Fig. (**7**(**a**)) for Ti/B_{51} and (**7**(**b**)) for Ti/B_{66}. After the first TDS peak (688 K), the Ti/B_{51} sample lost 22 % of the total hydrogen content. Two phases, namely hexagonal αTi (a = 0.295 nm, c = 0.469 nm) with an average crystallite size of about 20 nm and cubic TiH_{2-x}, x = 0.4, were detected in the corresponding XRD pattern, see Fig. (**7**(**a**)), curve 1. The hydride crystallite size was 16 nm at this stage. After the second TDS peak (812 K), the Ti/B_{51} sample lost 65% of total hydrogen content. Now, two hexagonal phases were detected in corresponding XRD pattern, see Fig. (**7**(**a**)), curve

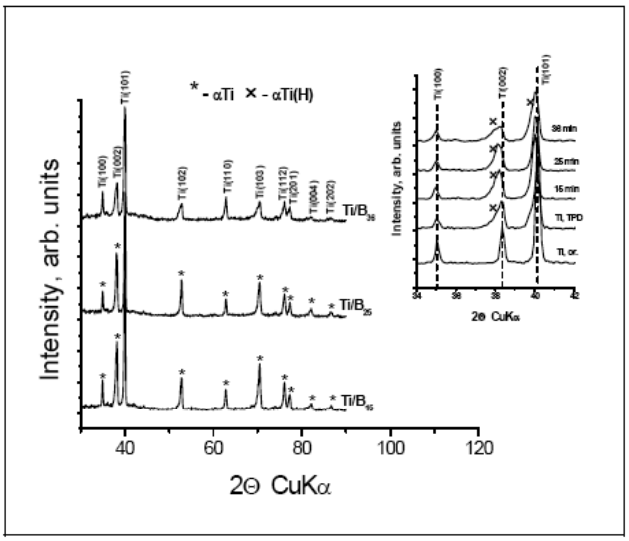

Fig. (6). XRD patterns recorded on early stages of Ti/B and H_2 interaction after TDS. Insert: details of Fig. (**6**). TPD: Temperature programmed desorption (= thermal desorption spectroscopy); Ti-or.: Titanium original.

2: αTi (a = 0.295 nm, c = 0.469 nm), with an average crystallite size of about 20 nm and a solid solution in Ti (a = 0.296 nm, c = 0.474 nm). Cubic TiH_{2-x}, x = 0.5, crystallite size about 30 nm, was left over in an amount of less then 10 wt. %. In case of the sample Ti/B_{66}, a hydrogen loss of 30 % was observed after the first TDS peak (680 K). Two major phases: 50 – 80 wt. % of cubic TiH_{2-x} (x = 0.5) with an average crystallite size of about 20 nm and αTi (a = 0.295 nm, c = 0.469 nm) with an average crystallite size of 50 – 70 nm were detected, see Fig. (**7**(**b**)), curve 1. After the second interrupted TDS (841 K), the sample lost 95 % of total hydrogen. As a result, only traces of Ti-hydride were detected. The major phase is a hexagonal phase (a = 0.296 nm, c = 0.475 nm) attributed to a solid solution in Ti. Additionally, some amount of αTi (a = 0.296 nm, c = 0.471 nm) can be detected. A special feature of these two XRD spectra is the background profile distortion between 2θ = 33 – 47°, which looks like an amorphous halo or the result of very wide overlapping peaks.

Figure. (**7**(**c**)) shows XRD patterns recorded after final TDS (1033 – 1046 K) for the samples Ti/B_{51}, Ti/B_{66} and Ti/B_{78}, respectively. These XRD patterns are best represented by a combination of two or three hexagonal phases. For Ti/B_{51}: about 40 wt % of αTi (a = 0.295 nm, c = 0.469 nm) and a solid solution in Ti (a = 0.296 nm, c = 0.474 nm). As for the samples Ti/B_{66} and Ti/B_{78}, only a small amount of αTi could be detected after TDS, see Fig. (**7**(**c**)), insert. A remarkable small-angle shift of XRD peaks shows the formation of a new hexagonal structure with lattice constant a similar to that of pure αTi and lattice constant c significantly larger (a = 0.297 nm, c = 0.477 – 0.479 nm). According to mass balance, after TDS the sample Ti/B_{66} contains less than 1 % of residual hydrogen and sample Ti/B_{78} is completely free of hydrogen.

Again, a background profile distortion between 2θ = 33 – 47°, which looks like amorphous halo or result of overlapping very wide peaks is clearly seen in Fig. (**7**(**c**)). The halo intensity increases in the range Ti/B_{51} → Ti/B_{66} →TiB_{78}. Very similar XRD patterns were obtained after TDS for Ti/B_{100} and as-milled TiH_2/B samples, see Fig. (**8**) and Table **4**: both consisted of a hexagonal phase with lattice constants being remarkably lager than pure αTi (a = 0.297 nm, c = 0.476 – 0.479 nm) and an amorphous halo between 2θ = 33 – 47°, which looks similar to the one observed in XRD spectra of

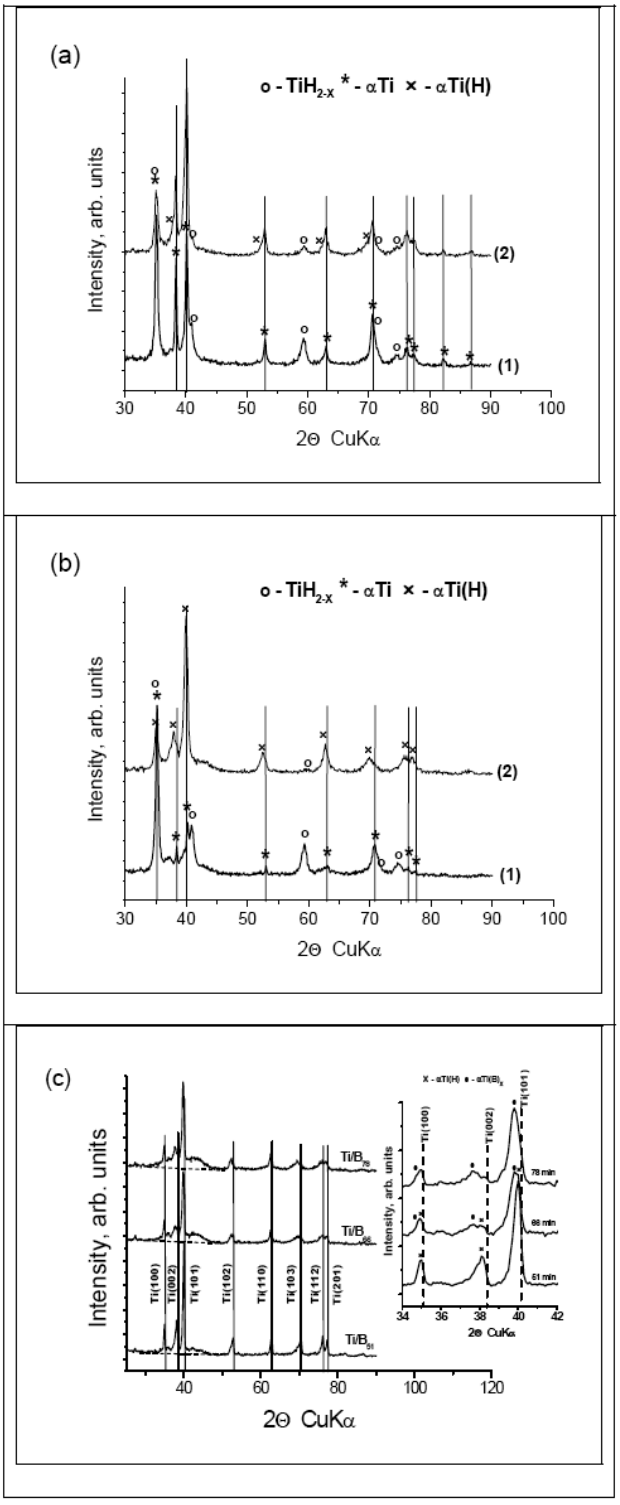

Fig. (7). XRD patterns recorded after TDS experiments depicted in Fig. (**6** (**b**)): (**a**) for Ti/B_{51} after 688 K (1) and 812 K(2); (**b**) for Ti/B_{66} after 680 K (1) and 841 K (2); (**c**) for Ti/B_{51}, Ti/B_{66} and Ti/B_{78}, respectively, after the total TDS. Insert: details of Fig. (**7** (**c**)).

TiB_{66} and Ti/B_{78} samples after TDS, compare Figs. (**7**(**c**) and **8**). In the case of Ti/B_{100}, the halo intensity is significantly higher than for TiH_2/B. Virtually no αTi was detected.

Table 4. Phase Compositions of Ti/B Powders After Interrupted and Total TDS

Sample	Treatment	Phases	Structure	Lattice Constants [nm]	
Ti/B_{15}	TDS	hex	αTi	a = 0.295	c = 0.469
		hex	αTi-5 at. % H	a = 0.296	c = 0.473
Ti/B_{25}	TDS	hex	αTi	a = 0.295	c = 0.470
		hex	αTi-3 at. % H	a = 0.2955	c = 0.471
Ti/B_{36}	TDS	hex	αTi	a = 0.295	c = 0.470
		hex	αTi-5.5 at. % H	a = 0.296	c = 0.474
Ti/B_{51}	TDS to 688 K	hex	αTi	a = 0.295	c = 0.469
		cub	δTiH_{2-x}	a = 0.4407	
	TDS to 812 K	hex	αTi	a = 0.295	c = 0.469
		hex	αTi-5.5 at. % H	a = 0.296	c = 0.474
		cub	δTiH_{2-x}	a = 0.4401	
	TDS	hex	αTi	a = 0.295	c = 0.469
		hex	αTi-5.5 at. % H	a = 0.296	c = 0.475
		halo			
Ti/B_{66}	TDS to 680 K	hex	αTi	a = 0.295	c = 0.469
		cub	δTiH_{2-x}	a = 0.4402	
	TDS to 841 K	hex	αTi	a = 0.296	c = 0.471
		hex	αTi-6.3 at. % H	a = 0.296	c = 0.475
		halo			
	TDS	hex	αTi(B)	a = 0.296 -	c = 0.473 -
		halo		0.298	0.480
Ti/B_{78}	TDS	hex	αTi(B)	a = 0.297	c = 0.477 -
		halo			0.479
Ti/B_{100}	TDS	hex	αTi(B)	a = 0.298	c = 0.475 -
		halo			0.480

hex = hexagonal; cub = cubic.

3.4. PAS Measurements

Table **5** shows the results of positron lifetime spectroscopy for initial B powder, Ti/B_{66}, Ti/B_{206}, and TiH_2/B ball milled in He atmosphere for 66 min. The symbols τ_i and I_i denote lifetimes and relative intensities of positron components. The last three columns in Table **5** are related to positronium contribution, which will be discussed in the following text. Estimated errors (1 standard deviation) are given in parenthesis. It was found that the initial B powder exhibits a single component PL spectrum (except of the source contribution) with lifetime $\tau_1 \approx 194$ ps. This testifies that virtually all positrons in the sample annihilate from one single state. The experimental lifetime τ_1 is remarkably longer than calculated bulk positron lifetime in B and even longer than the lifetime of positrons trapped at monovacancy in B, 163 ps [28]. This indicates that B powder contains open volume defects larger than monovacancies.

The PL spectra of Ti/B_{66} and Ti/B_{206} exhibit a short-lived and long-lived positron component besides a positronium (Ps) contribution. In porous media positrons can form Ps, i.e. a hydrogen-like binding state of a positron and an electron. A Ps atom having a size of about 0.1 nm is an ideal probe of nanoscopic pores. One can distinguish between singlet para-Ps (p-Ps) and triplet ortho-Ps (o-Ps) states which are formed in the ratio 1:3. In vacuum the lifetimes of p-Ps and o-Ps are 0.125 and 142 ns, respectively [29]. In solid material, however, the o-Ps lifetime is reduced due to pick-off annihilation with electrons of opposite spin from the surrounding medium. Due to spin exchange repulsion between the electron bound to the positron and core electrons, Ps is pushed into open holes. The probability of pick-off annihilation of o-Ps located in a nanoscopic hole depends on the overlap of the o-Ps wave function with the walls of the hole. Hence, o-Ps lifetime depends on the size of the hole. The mean lifetime of the o-Ps component $\tau_{o\text{-}Ps}$ and the size (width) $\sigma_{o\text{-}Ps}$ of distribution of o-Ps lifetimes are listed in Table **5** together with the intensity of the Ps contribution I_{Ps}. A p-Ps component with lifetime fixed at $\tau_{p\text{-}Ps} = 125$ ps and intensity $I_{p\text{-}Ps} = ¼\ I_{Ps}$ was assumed in fitting. The appearance of the Ps contribution in PL spectra of Ti/B and TiH_2/B specimens testify presence of nanoscopic pores, most probably localized at the Ti/B interfaces [28]. The lifetime of o-Ps component and the intensity of Ps contribution in Ti/B specimens decrease with increasing milling time, see Table **5**. The PL spectrum of TiH_2/B exhibits significantly lower intensity of Ps contribution, and a larger dispersion of o-Ps lifetime then the Ti/B specimens.

Table 5. Results of Positron Lifetime Spectroscopy

Sample	t_{mill} (min)	τ_1 (ps)	I_1 (%)	τ_2 (ps)	I_2 (%)	$\tau_{o\text{-}Ps}$ (ns)	$\sigma_{o\text{-}Ps}$ (ns)	I_{Ps} (%)
B powder	-	194.4(2)	100	-	-	-	-	-
Ti/B_{66}	66	173.3(6)	58.3(4)	344(3)	27.4(4)	1.89(1)	0.52(6)	14.3(2)
Ti/B_{206}	206	184(1)	55(1)	330(5)	37(1)	1.00(9)	0.60(9)	8(1)
TiH_2/B	66	193(1)	55.1(5)	348(2)	43.5(5)	1.75(5)	0.82(6)	1.48(4)

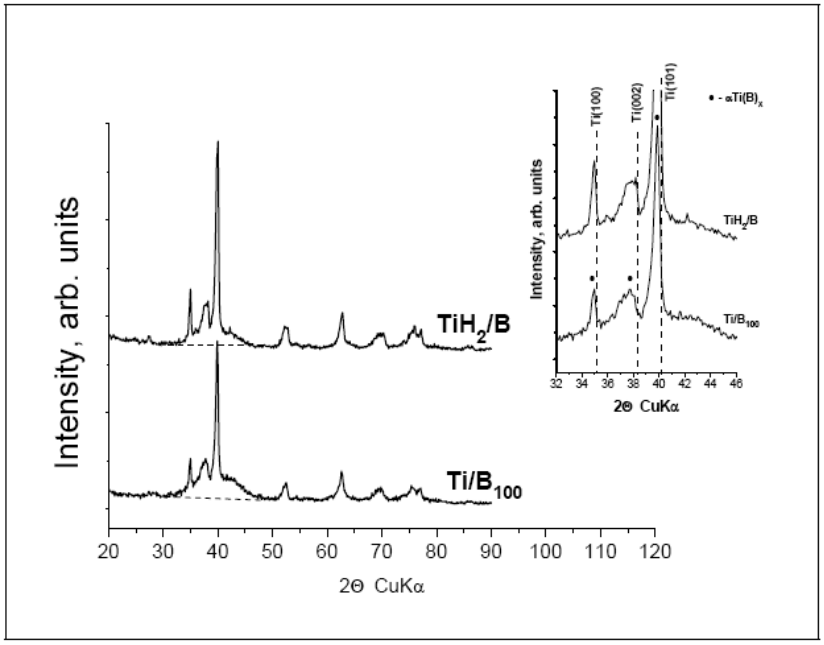

Fig. (8). XRD patterns recorded on final stage of Ti/B and H_2 interaction after TDS. Insert: details

3.5. XES Measurements

The results obtained by XES for Ti/B_{66} and Ti/B_{78} are presented in Fig. (**9**). Pure Ti, TiB_2, Ti/B mixture, TiH_2, and TiH_2/B, all milled for 66 min in He flow, are shown. Ti $L_{2,3}$ XES correspond to $3d4s \rightarrow 2p_{1/2,3/2}$ dipole transitions and probe occupied Ti *3d4s*-states. Ti $L_{2,3}$ XES has a rather simple structure which is formed by Ti-Ti bonds where Ti L_3 and Ti L_2-bands are separated by 6.4 eV, which corresponds to spin orbital splitting of Ti $2p_{3/2}$ and $2p_{1/2}$ core levels. In spectra of TiB_2 a low energy chemical shift of about 0.6 eV of the Ti $L_{2,3}$ XES takes place due to the shift of Ti *2p*-core levels. Ti $L_{2,3}$ XES of Ti/B, which corresponds to ball milling of Ti with B in He atmosphere, Ti-B bonds are formed, which is detected by the low energy chemical shift close to that of TiB_2. Ti $L_{2,3}$ XES of TiH_2 and TiH_2/B is characterized by an additional peak at 447.3 eV pointing to Ti-H bonds. The spectrum of Ti/B_{66} ball milled in H_2 atmosphere shows a slight peak at 447 eV and Ti $L_{2,3}$ peaks without a noticeable chemical shift. In contrast, Ti/B_{78} ball milled in H_2 atmosphere shows a pronounced Ti-H peak and a shift of the Ti $L_{2,3}$ peaks in the same direction as the Ti-B shift.

4. DISCUSSION

As follows from experimental data, Ti/B powder continuously changes in composition and morphology during the ball-milling treatment in H_2 flow. As a result, the original powder varies in composition from Ti/B to TiH_{2-x}/B which is closely accompanied by a change in mechanical properties. The large concentration of different surface defects generated during crushing of the Ti particles promotes H_2 dissociative chemisorption. However, the durability of these active sites is not evident: fresh Ti surface may be easily covered by Ti-hydride that locks the active sites, as was observed for pure Ti powder [27]. The prolonged post-milling sorption suggests that long-living active sites are localized not on Ti surface, but in positions, where no continuous titanium hydride layer can be formed, whereas hydrogen diffusion into the bulk goes rapidly. According to [27], it might be Ti/TiO_2 interfaces or grain boundaries: compare hydrogen diffusion coefficients in Ti at 303 K for grain boundary diffusion equal to 9.1 x 10^{-9} m^2/s [30] with that in bulk Ti and TiH_2 equal to 2.6 x 10^{-14} m^2/s [30] and 3.8 x 10^{-15} m^2/s [31], respectively. Ti-hydride nucleation goes preferably along the cracks and nearby structural defects because of the interaction of H atoms with bulk stress centers. According to [32-34], this process increases the density of strain-induced vacancies, which, in turn, leads to the formation of nanocracks and nanovoids. The latter promote additional Ti-hydride precipitation. Thus, the Ti-hydride emerging inside Ti nanocrystals is limited by two factors: (i) the propagation of bulk nanocracks and extended defects and (ii) the amount of H atoms introduced into the bulk. The observed prolonged Ti post milling charging can thus be explained by the durability of surface active sites responsible for H_2 dissociative chemisorption, and rapid bulk and grain boundary diffusion of H atoms in Ti [30], as well as additional precipitation of Ti-hydride inside Ti crystallites due to the propagation of inner cracks caused by Ti-hydride formation [32-34]. The powder size reduction exhibits two

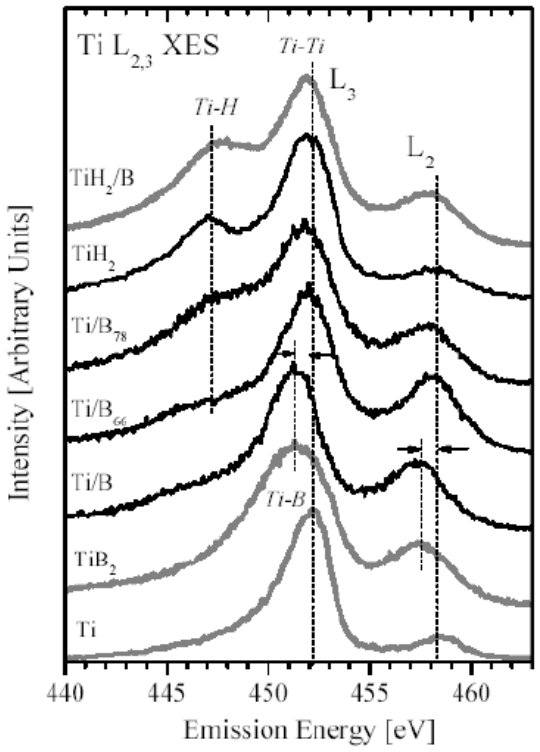

Fig. (9). Ti $L_{2,3}$ XES of Ti/B and TiH_2/B ball-milled nanocomposites.

regimes: a slow one for milling times up to 51 – 66 min, and a faster one for longer milling times, see Fig. (**10**), where the evolution of the specific surface area vs. milling time is plotted. Morphologically, the transition from slow to fast powder size reduction is accompanied by the formation of a homogeneous three-phase composition Ti/TiH_{2-x}/B, see Fig. (**1** (**c**), (**d**)), consisting of a boron matrix with Ti and/or Ti-hydride fragments of few nm in size randomly distributed, see Fig. (**2(b)**). At the transition, the hydride amount is 30 % (Ti/B_{51}) – 50 % (Ti/B_{66}), and the brittle hydride eases further powder size reduction. Moreover, the influence of the boron powder gets ever stronger, keeping Ti particles from agglomerating.

The fact that the desorption of pure Ti and of Ti/B_{15} exhibits only one high-temperature peak indicates that at this stage, only one type of site is available for H atoms, corresponding to hydrogen interstitials on tetrahedral positions in the Ti lattice. After prolonged milling, low-temperature peaks appear, indicating that new occupation sites are available for hydrogen after milling. The fact that pure Ti, milled for 66 min in H_2 flow exhibits only the high-temperature peak indicates that the presence of boron plays a crucial role in the generation of new occupation sites. Fig. (**11**) shows the amount of hydrogen desorbed vs. the desorption temperature for the samples milled with boron for different milling times. The results for Ti/B_{25} may not be very meaningful because the absolute amount of desorbed hydrogen is very small, and will not be discussed in the following. As for the other samples, four groups of peaks can be distinguished: (i) a high-temperature peak at about 950 K corresponding to the single peak observed for pure Ti and Ti/B_{15}, which disappears after 66 min of milling, (ii) a peak at about 850 K, (iii) a peak at 750 – 800 K, and (iv) a low-temperature peak at 600 – 650 K that appears only after 51 min of milling. The high-temperature peak can be associated with hydrogen in bulk sites in Ti. After 66 min of milling, when this desorption peak disappears, no α-Ti is detected in XRD, corroborating this interpretation. The

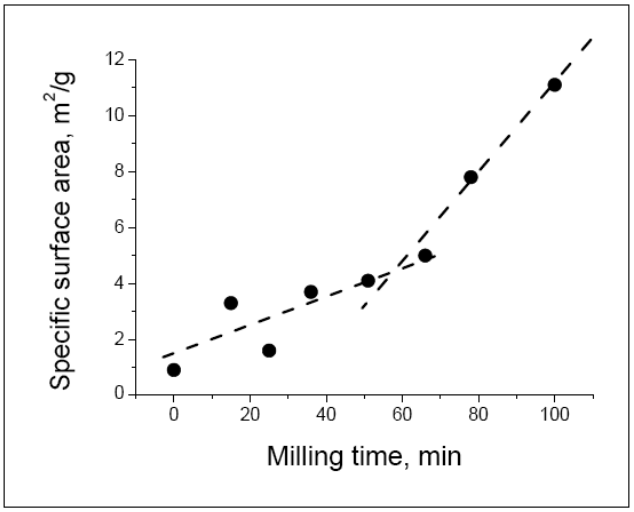

Fig. (10). Specific surface area of Ti/B ball milled composites.

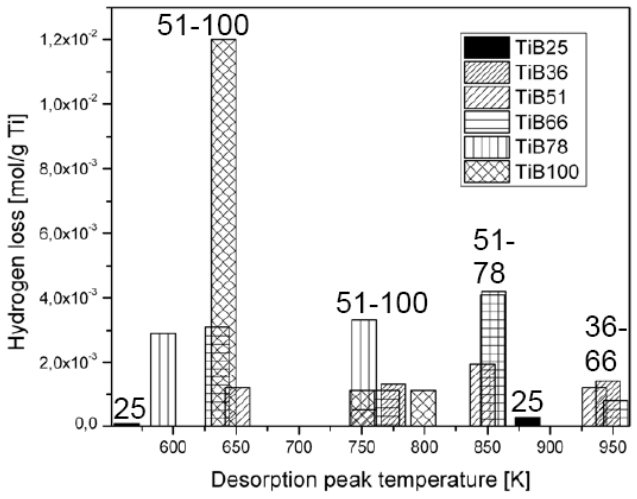

Fig. (11). Hydrogen evolution during TDS vs. desorption peak temperature of Ti/B ball milled composites. The numbers (e.g. 51-100) give the range of milling times in minutes for each of the desorption temperature clusters.

peaks at 850 K and 750 – 800 K can be attributed to the desorption of hydrogen from TiH_{2-x} unaltered by boron, since TiH_2 exhibits two prominent desorption peaks in these temperature ranges [35]. The low-temperature peaks, finally, stem from sites that are present due to interaction with boron. It should be noted that the vanishing of the high-temperature peak and the appearance of the low-temperature peak coincide with the transition from slow to fast powder size reduction.

The role of the boron additive is versatile: One task is to prevent the Ti particles from sticking together easing hydrogen sorption by offering short diffusion lengths. Another one is to form a matrix accommodating the nanoscopic Ti, later TiH_{2-x} particles. Here, the boron also prevents the fresh Ti surface from forming an oxide layer, further easing H sorption. However, two additional features related to boron promote the formation of low-temperature desorption peaks: the formation of nanoscopic holes available for hydrogen, and an interstitial solution of boron in the TiH_{2-x}. Both issues will be discussed in the following.

One possible cause for weakly bound hydrogen associated with low desorption temperatures was found with PAS. The lifetime

determined experimentally in initial B powder, (194.4 ± 2) ps, is comparable to the lifetime calculated for positrons trapped at di-vacancies in B [28]. Note that even longer positron lifetime of (243 ± 5) ps was measured on commercial B powder in Ref. [36]. Unfortunately no details about this powder were mentioned. However, it is likely that the B powder investigated in Ref. [36] contains larger vacancy clusters than the B powder studied in this work. In case of milled Ti/B and TiH_2/B composites, nanoscopic holes were found. In Table **6**, parameters related to the free volume size in Ti/B nanocomposites ball milled in H_2/He effluent gas and TiH_2/B nanocomposite ball milled in He atmosphere are listed. The nanocomposites were ball milled for the period t_{mill}. The symbols R_{mean} and V_{mean}, respectively, denote the mean radius and volume of pores. The PL results suggest that the size of nanoscopic pores in Ti/B nanocomposites decreases with milling time. This is indicated by a decrease in the probability of Ps formation reflected by a drop in intensity of the Ps component I_{Ps}, see Table **5**. This effect can be explained by an increased level of intermixing of Ti particles with boron additive, which leads to a reduction of pore sizes; and/or a filling of nanoscopic pores by hydrogen, which is absorbed in and Ti/B nanocomposites. Hydrogen can be present inside the nanoscopic pores either absorbed on the inner surfaces of the pores or in form of H_2 molecules. It seems logical to assume that hydrogen stored in these nanoscopic holes in either way will be desorbed at substantially lower temperatures than hydrogen stored in TiH_{2-x} or in interstitial sites in Ti. Since Ti/B_{100} desorbed much more hydrogen from these sites than Ti/B_{51-78}, it also seems logical to assume that the nanoscopic holes do not decrease in size but rather get filled with hydrogen, making the holes appear smaller for Ps. Additionally, it seems obvious that the appearance of the nanoscopic holes is related to the presence of boron. They are most probably situated at the Ti-B interfaces [28]. The size of the nanopores as given in Table **6** is rather small which makes it unlikely that more than one or two hydrogen atoms or molecules are situated in each one of them. It can therefore be concluded that by no means all of the hydrogen is stored in these nanopores.

Table 6. Parameters Related to the Free Volume Size in Ti/B Nano-composites

Sample	t_{mill} (h)	R_{mean} (nm)	V_{mean} (nm^3)
Ti/B_{66}	66	0.27(2)	0.082(8)
Ti/B_{206}	206	0.12(1)	0.008(6)
TiH_2/B	66	0.24(3)	0.059(8)

As follows from XES data, which gives detailed information about the local atomic and electronic structure of Ti and B atoms, boron atoms change the local bonding structure of Ti in the Ti/TiH_{2-x}/B nanocomposites. In case of Ti/B_{78} a pronounced Ti-H peak and a shift of the Ti $L_{2,3}$ peaks in the same direction as the Ti-B shift are observed. This is not the case for Ti/B_{66}. When TiH_2/B or Ti/B are milled in He for 66 min, the same chemical shift is observed. Therefore, one can conclude that Ti-B interaction takes place only when Ti-H bonds are saturated. The mechanical activation in H_2/He gives preference for the formation of Ti-H bonds. When these bonds are saturated after the formation of TiH_{2-x} an incorporation of B atoms to TiH_2 lattice and the formation of additional Ti-B bonds take place.

This leads to the other major effect of the powder evolution, i.e. the introduction of boron atoms into the Ti and/or TiH_2 lattice, which was detected by XRD measurements, see Figs. (**7**(**c**) and **8**). A significant increase in lattice parameters of the hexagonal phase after desorption was observed and a remarkable broadening of Ti(002), Ti(110) and Ti(103) peaks, which indicates a solid solution αTi(B). Partially amorphous or extremely fine Ti or TiB-containing phases are observed for Ti/B_{100}, and to a lesser extent, for Ti/B_{51-78} nanocomposites after TDS heating. These phases are, evidently, responsible for the amorphous halo, because the most intensive peaks of hexagonal αTi or αTi(B) solid solution, cubic TiB (calculated phase [19]) and hexagonal TiB_2 (JSPDS 35-741) phases are localized just in this angle range. In support of this conjecture, only TiB and TiB_2 were detected after Ti/B_{100} powder was heated up to 1473 K. In this case, no background profile distortion was observed. The content of boron dissolved interstitially can be estimated as more then 18 at. %. From equilibrium Ti – B phase diagram [37], boron solubility in Ti is less than 0.1 at. %. It seems likely that that those boron atoms are introduced not in titanium, but in Ti-hydride lattice upon the mechanical impact, which is in accordance with Hägg's rule [38]. That is, simple interstitial phases can form when the ratio between radii of nonmetal (R_n) and metal (R_m) atoms is $R_n/R_m \leq 0.59$. Thus, the introduction of B (R_B = 0.091 nm [39]) atoms in Ti (R_{Ti} = 0.154 nm [38]) lattice is forbidden, because of R_B/R_{Ti} = 0.62. However, in the case of TiH_2 (structural type CaF_2) with lattice constant a = 0.444 nm (see Table **2**), the entry of B atoms becomes possible due to an effective R_{Ti} = 0.157 nm and R_B/R_{Ti} = 0.58. This suggestion is also based on our previous study concerning mechanically induced modification of TiH_2 by boron atoms in TiH_2/B system [40].

In all samples except Ti/B_{78}, there seems to be residual hydrogen up to 10 %. It can be assumed that residual hydrogen is interstitially dissolved in Ti lattice. In case of Ti/B_{66-100}, the *c*-axis of the hexagonal phase(s) after TDS gives rise to broad reflections, which can well be associated with two hexagonal solid solutions, one of which is Ti(B), and the other Ti(H).

5. CONCLUSIONS

The mechanically induced transformations in Ti/B/H_2 system are described as a two-stage process. Each stage is described in the framework of both chemical and morphological transformations, as follows:

On early stages of intermixing of Ti and B powders, hydrogen is situated at interstitial positions in Ti characterized by high thermal stability, T_{max} = 946 – 1000 K, a peak that disappears after 66 min of milling This is followed by a progressive increase in δTiH_{2-x} content together with the transformation of Ti/TiH_{2-x}/B to a nanocomposite consisting of a boron matrix with embedded Ti and TiH_{2-x} nanofragments. Two new desorption peaks emerge, at T_{max} = 850 K and T_{max} = 750 – 800 K, characteristic for the decomposition of TiH_2.

The second stage begins after 51-66 min of milling. In this stage, the powder size reduction was markedly faster than in the first stage, and a new low-temperature peak emerges at T_{max} = 600 – 650 K. This peak is the result of boron interaction with the powders. On the one hand, nanosized pores appear that contain weakly bound hydrogen, and on the other hand, boron is introduced into the TiH_{2-x} lattice, where it modifies the bonding structure of Ti, hereby lowering the binding energy of hydrogen in the hydride.

ACKNOWLEDGEMENTS

This work was done with partial support of RFBR (Project No. 10-03-00942-a), the Research Council of the President of the Russian Federation (Grant No. NSH-3572.2010.2), the Russian Science Foundation for Basic Research (Project No. 08-02-00148), the Ministry of Education, Youth, and Sports of the Czech Republic (Project No. MS 0021620834) and the Academy of Science of Czech Republic (Project No. KAN300100801). We gratefully acknowledge support from the Natural Sciences and Engineering.

REFERENCES

[1] Calka, A. Formation of titanium and zirkonium nitrides by mechanical alloying. *Appl. Phys. Lett.,* **1991**, *59*, 1568-1569.

[2] Memezawa, A.; Aoki, K.; Masumoto, T. Amorphization of Ti-Zr powders by the collaborated interaction of mechanical alloying and hydrogenation. *Scripta Met. Mat.*, **1993**, *128*, 361-365.

[3] Zhang, H.; Kisi, E.H. Formation of titanium hydride at room temperature by ball milling. *J. Phys. Condens. Matter*, **1997**, *9*, L185-L190.

[4] Streletskii, A.N.; Morozova, O.S.; Berestetskaya, I.V.; Borunova, A.V. Hydrogenation of CO and C during mechanical treatment of Zr and Ni containing systems. *Mater. Sci. Forum*, **1998**, *269-270*, 283-288.

[5] Small, D.A.; MacKey, G.R.; Dunlap, R.A. Hydriding reactions in ball-milled titanium. *J. Alloys Comp*., **1998**, *284*, 312-315.

[6] Bobet, J.-L.; Even, C.; Quenisset, J.-M. On the production of ultra-fine grained titanium hydride powder at room temperature. *J. Alloys Comp.*, **2003**, *348*, 247-251.

[7] Suryanarayana, C. Mechanical alloying and milling. *Progr. Mater. Sci.*, **2001**, *46*, 1-184.

[8] Zaluska, A.; Zaluski, L.; Ström-Olsen, J.O. Sodium alanates for reversible hydrogen storage. *J. Alloys Comp.*, **2000**, *298*, 125-134.

[9] Bogdanović, B.; Schwickardi, M. Ti-doped alkali metal aluminium hydrides as potential novel reversible hydrogen storage materials. *J. Alloys Comp.*, **1997**, *253*, 1-9.

[10] Byun, J.-S.; Shim, J.-H.; Cho, Y.W. Influence of stearic acid on mechanochemical reaction between Ti and BN powders. *J. Alloys Comp.*, **2004**, *365*, 149-156.

[11] MacKey, G.R. *Hydrogen Compounds of the Metallic Elements*, Spon, London, **1965**.

[12] Borchers, C.; Leonov, A.V.; Khomenko, T.I.; Morozova, O.S. Stimulating effect of graphite admixture on hydrogen sorption-desorption properties of mechanically activated titanium powder. *J. Phys. Chem. B*, **2005**, *109*, 10341-10347.

[13] Borchers, C.; Khomenko, T.I.; Morozova, O.S.; Galakhov, A.V.; Kurmaev, E.Z.; McNaughton, J.; Yabloskikh, M.V.; Moewes, A. Influence of graphite addition on the reactivity of Ti powder with H_2 under ball milling. *J. Phys. Chem. B*, **2006**, *110*, 196-204.

[14] Dobrovol'skii, V.D.; Radchenko, O.G.; Solonin, Y.M.; Muratov, V.B.; Morozov, I.A. Effect of dispersal and mechanical boron alloying on the thermal stability of hydride phases in the Ti-B-H system. *Powder Metal. Metal Ceram.*, **2006**, *45*, 485-492.

[15] Fang, Z.Z.; Ma, L.P.; Kang, X.D.; Wang, P.J.; Wang, P.; Cheng, H.M. In situ formation and rapid decomposition of $Ti(BH_4)_3$ by by mechanical milling $LiBH_4$ with TiF_3. *Appl. Phys. Lett.*, **2009**, *94*, 044104.

[16] Marks, T.J.; Kolb, J.R. Covalent transition metal, lanthanide, and actinide tetrahydroborate complexes. *Chem. Rev.*, **1977**, *77*, 263-293.

[17] San-Martin, A.; Manchester, F.D. The H–Ti (Hydrogen-Titanium) system. *Bull. Alloy Phase Diag*,. **1987**, *8*, 30-42.

[18] Mirkin, A.I. *Handbook on X-ray Diffraction Analysis of Polycrystals*, Nauka: Moscow, **1961** (in Russian).

[19] Shelekhov, E.V.; Sviridova, T.A. Programs for X-ray analysis of polycrystals. *Metal Sci. Heat Treatment*, **2000**, *42*, 309-313.

[20] Warren, B.E. X-ray studies of deformed metals. *Prog. Metal. Phys*., **1959**, *8*, 147-202.

[21] Krishnan, R. X-Ray Studies on Cold-Worked HCP Metals and Alloys. *Z. Metallkunde*, **1967**, *58*, 811-813.

[22] Pilyankevich, E.A. Diffraction effects defined by strong one-dimensional disorder in hcp structures. *Kristallografiya*, **1986**, *31*, 55-59.

[23] Becvar, F.; Cızek, J.; Prochazka, I.; Janotova, J. The asset of ultra-fast digitizers for positron-lifetime spectroscopy *Nucl. Instrum. Methods A*, **2005**, *539*, 372-385.

[24] Becvar, F.; Cizek, J.; Prochazka, I. High-resolution positron lifetime measurement using ultra fast digitizers Acqiris DC211 *Appl. Surf. Sci*., **2008**, *255*, 111-114.

[25] Becvar, F. Methodology of positron lifetime spectroscopy: Present status and perspectives *Nucl. Instrum. Methods* B, **2007**, *261*, 871-874.

[26] Kansy, J. Microcomputer program for analysis of positron annihilation lifetime spectra. *Nucl. Instrum. Methods A*, **1996**, *374*, 235-244.

[27] Borchers, C.; Morozova, O.S.; Khomenko, T.I. ; Leonov, A.V.; Postnikov, A.V.; Kurmaev, E.Z.; Moewes, A.; Pundt, A. Effect of *h*-BN Additive on Hydrogen Sorption by Ti under Mechanical Treatment in H_2/He Flow. *J. Phys. Chem. C*, **2008**, *112*, 5869-5879.

[28] Cizek, J.; Prochazka, I.; Morozova, O.S.; Borchers, C.; Pundt, A. Size distribution of nanoscopic holes in Ti/*h*-BN and Ti/B nanocomposites. *J. Appl. Phys.* **2010**, *107*, 043509.

[29] Mogensen, O.E. *Positron Annihilation in Chemistry*, Springer: Berlin, **1995**.

[30] Abdul-Hamid, O.S. *Diffusion of hydrogen in Titanium*. PhD Thesis, Cambridge, MA, **1993**.

[31] Mizuno, K.; Furuya, Y.; Hirano, K.; Okamoto, H. Hydrogen diffusion in titanium-hydride observed by the diffraction-enhanced X-ray imaging method. *Phys. Stat. Sol. A*, **2007**, *204*, 2734-2739.

[32] Shich, D.S.; Robertson, I.M.; Birnbaum, H.K. Hydrogen embrittlement of alpha-titanium - insitu tem studies. *Acta Metall.*, **1988**, *36*, 111-124.

[33] Birnbaum, H.K.; Sofronis, P. Hydrogen-enhanced localized plasticity - a mechanism for hydrogen-related fracture. *Mater. Sci. Engr. A*, **1993**, *176*, 191-202.

[34] Robertson, I.M. The effect of hydrogen on dislocation dynamics. *Engr. Fracture Mechanics*, **2001**, *68*, 671-692.

[35] Borchers, C.; Khomenko, T.I.; Leonov, A.V.; Morozova, O.S. Interrupted thermal desorption of TiH_2. *Thermochim. Acta*, **2009**, *493*, 80-84.

[36] Pujari, P.K.; Sudarshan, K.; Goswami, A.; Manohar, S.B.; Aswal, D.K.; Singh, A.; Sen, S.; Gupta, S.K. Positron annihilation studies in the MgB_2 superconductor**.** *Phys. Rev. B*, **2002**, *66*, 012518.

[37] Massalski, T.B. *Binary Alloy Phase Diagrams*. ASM International: Materials Park, OH, **1990**, 544.

[38] Hägg, G. Eigenschaften der Phasen von Übergangselementen in binären Systemen mit Bor, Kohlenstoff und Stickstoff. *Phys. Chem. B,* **1929**, *6*, 221-232 (in German).

[39] Chang, R. *Essential Chemistry*, www.mhhe.com/physsci/chemistry/ essentialchemistry/flash/**atomic**4.swf, (accessed March 22, **2011**).

[40] Morozova, O.S.; Khomenko, T.I.; Borchers, C.; Leonov, A.V.; Kurmaev, E.Z.; Moewes, A. Effect of N, C and B interstitial atoms on local bonding structure in mechanically activated TiH_2/h-BN, TiH_2/C, and TiH_2/B mixtures. *J. Alloys Comp*., **2009**, *483*, 309-312.

Received: March 22, 2011 Revised: May 20, 2011 Accepted: June 6, 2011